Plasmonic Enhancement of Raman Optical Activity in Molecules near Metal Nanoshells[†]

Ramiro Acevedo,[‡,§,||,⊥] Richard Lombardini,[‡,§,||] Naomi J. Halas,[‡,§,||,#] and Bruce R. Johnson*[,‡,§,||]

Department of Chemistry, Rice Quantum Institute, Laboratory for NanoPhotonics, Applied Physics Program, and Department of Electrical and Computer Engineering, MS 60, Rice University, Houston, Texas 77005

Received: April 22, 2009; Revised Manuscript Received: June 10, 2009

Surface-enhanced Raman optical activity (SEROA) is investigated theoretically for molecules near a metal nanoshell. For this purpose, induced molecular electric dipole, magnetic dipole, and electric quadrupole moments must all be included. The incident field and the induced multipole fields all scatter from the nanoshell, and the scattered waves can be calculated via extended Mie theory. It is straightforward in this framework to calculate the incident frequency dependence of SEROA intensities, i.e., SEROA excitation profiles. The differential Raman scattering is examined in detail for a simple chiroptical model that provides analytical forms for the relevant dynamical molecular response tensors. This allows a detailed investigation into circumstances that simultaneously provide strong enhancement of differential intensities and remain selective for molecules with chirality.

I. Introduction

Metal nanoparticles supporting surface plasmon modes of the conduction electrons are capable of strongly modifying the spectroscopy of attached or nearby molecules. A leading example is surface-enhanced Raman scattering (SERS),[1−4] for which the inelastic Raman cross-section is typically several orders of magnitude higher than in the absence of the plasmonic particle. This enhances the usefulness of Raman scattering as a vibrational spectroscopy, e.g., for chemical and biomolecule analysis and sensing.[5,6] Raman optical activity[7,8] (ROA), which is exhibited in differences between right- and left-circularly polarized Raman-scattering intensities, provides a spectroscopy that is sensitive to chirality in molecules and that would similarly benefit from development of a surface-enhanced version (SEROA).[9−20] However, ROA depends on subtle interplay between the electric dipole ($E1$) moment of the molecule and its magnetic dipole ($M1$) and electric quadrupole ($E2$) moments, and much work will be needed to understand precisely how this interplay is affected by the strong local electromagnetic (EM) fields near nanoparticles of silver, gold, and other metals.

Here this question is examined in detail for the particular situation of chiral molecules moving near spherical metal nanoshells with dielectric cores.[21] For such a scenario, it is possible to extend and merge the classical-fields model of SERS by Kerker, Wang, and Chew[22] (KWC) and the off-resonant formalism for ROA by Barron and Buckingham.[7] The resulting formalism allows prediction of SEROA circular intensity differences (CIDs) and their enhancements as functions of excitation frequency in terms of the dynamic ROA response tensors. In conjunction with a recent chiroptical orbital model,[23] it is also shown to allow an investigation of particular circumstances where SEROA retains the selectivity of ROA to molecules with chiral symmetry.

ROA spectroscopy is valuable in analyzing higher structure in proteins, viruses and chiral molecules.[8,24] For gas or solution ensembles of molecules, averaging over orientations erases CIDs except when the molecules have chiral character. Then intensity cross-terms between molecular response tensors ($E1/M1$ and $E1/E2$) provide the leading nonvanishing contributions to the CIDs and are sensitive to such things as the relative proportions of α-helix and β-sheet conformations in specific proteins.[24] However, the differential Raman scattering cross sections are quite small. While ordinary CIDs today may be measured in less than 1 h, very small CIDs still require days to acquire measurements with an adequate signal-to-noise ratio.

The possibility of vastly increasing data acquisition rates has thus drawn attention to implementation of SEROA,[9−20,25] which was suggested many years ago by Efrima.[9,10] A recent detailed theoretical investigation has been performed by Janesko and Scuseria,[15] who specifically consider the effects of averaging over nanoparticle/molecule orientations as well as concomitant selection rules and scaling behavior. An experimental investigation by Kneipp et al.[13] measured CIDs for adenine on silver colloids, suggesting that the molecule, while achiral by itself, forms a chiral complex with the silver surface. Further exploratory investigations of SEROA are described by Abdali and Blanch.[20] There has been debate about whether or not CIDs in SEROA measurements will be attributable specifically to chiral molecules. For instance, Etchegoin et al.[16] point out that SERS can be dominated by molecules in "hot spots" between neighboring colloidal particles, so that polarization measurements will primarily reflect the electric-vector alignment with the interparticle axis and chiral-molecule contributions to differential Raman scattering signals will be essentially unmeasurable. There is much remaining to be understood in SEROA CIDs for adsorbed molecules, given the complex environments that may occur. This is not surprising since even SERS has a long history of continuing debates for adsorbed molecules, e.g., electromagnetic versus chemical effect enhancement contributions.[3,4,26] The present theoretical investigation addresses a situation of intermediate complexity where EM enhancement is expected to dominate.

[†] Part of the "Robert W. Field Festschrift".

* To whom correspondence should be addressed.

[‡] Department of Chemistry.

[§] Rice Quantum Institute.

[||] Laboratory for NanoPhotonics.

[⊥] Applied Physics Program.

[#] Department of Electrical and Computer Engineering.

10.1021/jp9037232 CCC: $40.75

The KWC picture of off-resonant SERS[22] considers a molecule near a silver nanosphere exposed to both an external plane-wave field and its secondary wave scattered from the nanosphere. The total local field induces an electric dipole in the molecule that may be described as a radiating classical dipole, and the latter radiation also scatters from the nanosphere. Both absorption and emission processes are enhanced, leading to a well-known product form for the full SERS enhancement. For SEROA, it is necessary to also consider induced $M1$ and $E2$ molecular moments as well as their equivalent classical fields and concomitant scattering from the nanoparticles. The KWC uses of Mie theory[27,28] and the dyadic Green tensor for the EM field[22,29,30] are further generalized for these purposes, and it is found that the different multipole scattering problems are each fully determined in terms of the usual Mie coefficients calculated at the Raman-shifted frequency. For application to nanoshells instead of nanospheres, it is only necessary to use the appropriate Mie coefficients.[31]

It is found that different individual molecular multipoles have different enhancement curves as functions of excitation frequency/wavelength. In order to include wavelength dependence of the response tensors as well as inherent chirality of the molecule, the twisted-arc model[23] of delocalized electron orbitals in H_2S_2 is used as a qualitative tool. This "wire-frame" model defines one-electron orbitals along two joined arcs twisted with respect to each other by the dihedral angle χ of the molecule, providing simple χ-parametrized matrix elements and response tensors. Within this spectral SEROA model, the differences from ROA can be investigated in detail. It is verified that averaging over molecular rotational coordinates, which suffices to make ROA selective for chirality, is not sufficient to achieve the same thing in SEROA. On the other hand, focusing on the configuration of a backscatter instrument built for SEROA measurements at Rice University,[25] it is determined that additional averaging of molecular positions around the nanoshell (see also Janesko and Scuseria[15]) serves to guarantee chiral selectivity. Other configurations can be investigated with the same model, but this shows that there are indeed circumstances where it is possible to retain the selectivity while achieving enhancement.

II. Raman Optical Activity near Plasmonic Scatterers

A. Unenhanced ROA. Assuming a monochromatic EM field of frequency ω_0 in spectral regions where the molecule is transparent, the description of ordinary nonresonant ROA uses the complex induced $E1$, $M1$, $E2$ multipole moments (electric dipole $\mathbf{d}$, magnetic dipole $\mathbf{m}$, and electric quadrupole $\boldsymbol{\Theta}$) of the molecule[7,32]

$$d_j = \alpha_{jk}E_k + G_{jk}B_k + \frac{1}{3}A_{jkl}\frac{\partial}{\partial x_k}E_l + ... \tag{1}$$

$$m_j = G_{kj}^{*}E_k + ... \tag{2}$$

$$\Theta_{jk} = A_{ljk}^{*}E_l + ... \tag{3}$$

[See eqs 2.6.34 of ref 32, where tildes are used to distinguish these generally complex quantities.] A repeated index summation convention is used in eqs 1−3, and MKS units are employed throughout. The α_{jk} are elements of the electric dipole-electric dipole polarizability tensor $\boldsymbol{\alpha}$, the G_{jk} are those of the electric dipole-magnetic dipole optical activity tensor $\mathbf{G}$, and the A_{jkl} are those of the electric dipole-electric quadrupole optical activity tensor $\mathbf{A}$. If the wave functions may be taken as real, then $\boldsymbol{\alpha}$ and $\mathbf{A}$ are real and $\mathbf{G} = -i\mathbf{G}'$ is imaginary.[33] The incident electric field $\mathbf{E}$ and magnetic field $\mathbf{B}$ both depend on frequency ω_0 and position $\mathbf{r}$, this dependence being simplest in the case of a plane wave. It is assumed that these fields correspond to $e^{-i\omega_0 t}$ time behavior.

In a classical field picture, the molecule supports radiating $E1$, $M1$, and $E2$ multipole fields[34] that, for Raman scattering, oscillate at a frequency ω shifted from ω_0 by a vibrational quantum. Thus, for example, there is an EM field with vectors $\mathbf{E}^{(E1)}(\omega,\mathbf{r})$ and $\mathbf{B}^{(E1)}(\omega,\mathbf{r})$ generated from $\mathbf{d}$, as well as corresponding fields generated by $\mathbf{m}$ and the electric quadrupole tensor. These are detailed by Jackson,[34] who uses a quadrupole tensor $\mathbf{Q}$ that is twice the tensor $\boldsymbol{\Theta}$ used by Barron and Buckingham.[7]

In the electric dipole approximation, only $\mathbf{d}$ is considered and only the $\boldsymbol{\alpha}\cdot\mathbf{E}$ contribution to it in eq 1 is included. For ROA, however, it is necessary to include the other contributions to the multipole moments shown in eq 1 and to include the other radiating multipole fields. If the oscillating moments are regarded quantum mechanically, time-dependent perturbation theory yields sum-over-intermediate-states forms for all of the response tensors.[7] These involve products of absorption and emission transition matrix elements (in off-resonant virtual-state terminology), and those where both matrix elements are of the electric dipole operator ($\boldsymbol{\alpha}$) dominate the total intensities.

The intensities can be calculated from components of the (cycle-averaged) Poynting vector

$$\mathbf{S} = \frac{1}{2\mu_0}Re(\mathbf{E}_{\mathrm{rad}} \times \mathbf{B}_{\mathrm{rad}}^{*}) \tag{4}$$

where

$$\mathbf{E}_{\mathrm{rad}} = \mathbf{E}^{(E1)} + \mathbf{E}^{(M1)} + \mathbf{E}^{(E2)} + ... \tag{5}$$

and similarly for $\mathbf{B}_{\mathrm{rad}}$. Here μ_0 is the free-space magnetic permeability. Barron and Buckingham derived explicit expressions for intensity differences with plane-wave excitation using the asymptotic forms for the fields.[7] For example, with an initial CW field of amplitude E_0 propagating along z and having either right or left circular polarization vectors $(\hat{x} \mp i\hat{y})/\sqrt{2}$, the ICP (incident circular polarization) difference in x-polarized Rayleigh intensities detected at distance r along y is calculated to leading orders as

$$S_x^{\mathrm{R}} - S_x^{\mathrm{L}} = \frac{\omega_0^4 u_0 E_0^2}{16\pi^2 c^2 r^2}\Big\langle Im(c\alpha_{xy}\alpha_{xx}^{*} + \alpha_{xy}G_{xy}^{*} + \alpha_{xx}G_{xx}^{*} + \alpha_{xy}G_{xz}^{*} - \alpha_{xx}G_{yz}^{*}) + \frac{\omega_0}{3}Re(\alpha_{xx}A_{xzy}^{*} - \alpha_{xy}A_{xzx}^{*} + \alpha_{xy}A_{xxy}^{*} - \alpha_{xx}A_{yxy}^{*})\Big\rangle \tag{6}$$

where c is the speed of light. The angular brackets indicate orientational averaging, appropriate for randomly oriented molecules in gas or solution phase. The averaging is accomplished by standard integration of products of direction cosine matrix elements, and leads to vanishing of any "αα" contributions (i.e., averages over products of $\boldsymbol{\alpha}$ tensor elements) to intensity differences. However, nonzero αG and αA contributions are still obtained for molecules that have chiral symmetry.

These are typically $10^{-3}-10^{-5}$ times the total (nondifferential) intensity,[15] requiring long ROA data acquisition times.

Luber et al.[35] have recently reviewed earlier investigations of the relative sizes of the αG and αA cross terms in unenhanced ROA and performed a density functional theory analysis across a series of organic compounds including alkanes, alkenes, amino acids, and larger peptides. With exceptions of certain C−H stretching modes, the calculated ROA spectra were little-changed when the αA terms were neglected. These are the most difficult terms to calculate, so neglecting them would simplify ab initio spectral simulations.

B. Enhanced ROA. In the presence of a metal nanoparticle supporting surface plasmons, the situation changes considerably. Even if the molecule is not in direct contact, local field enhancements strongly modify the Raman scattering and must be included in the scattering formalism. For the simplest case of spherical metal particles in the electric dipole approximation, this has been accomplished in the Mie theory investigation by KWC.[22] First, the induced dipole is calculated as $\mathbf{d} = \alpha\cdot(\mathbf{E} + \mathbf{E}_s) = \alpha\cdot\mathbf{E}_t$ where $\mathbf{E}_s$ is the wave produced when the plane wave $\mathbf{E}$ scatters from the nanoparticle. The resulting dipole $\mathbf{d}$ then emits an electric field $\mathbf{E}^{(E1)}$ that can be associated with a classical electric dipole oscillating at the Raman-shifted frequency ω. This field also scatters from the nanoparticle and produces the field $\mathbf{E}_s^{(E1)}$. The total Raman-shifted field intensity observed at position $\mathbf{r}$ is then proportional to $r^2|\mathbf{E}^{(E1)}(\mathbf{r}) + \mathbf{E}_s^{(E1)}(\mathbf{r})|^2$.

Generalizing the KWC model to include higher molecular multipoles, we have (the symbol : is used for double tensor contraction)

$$\mathbf{d} = \alpha\cdot(\mathbf{E} + \mathbf{E}_s) + \mathbf{G}\cdot(\mathbf{B} + \mathbf{B}_s) + \frac{1}{3}\mathbf{A}:\nabla(\mathbf{E} + \mathbf{E}_s) + ... \tag{7}$$

$$\mathbf{m} = (\mathbf{E} + \mathbf{E}_s)\cdot\mathbf{G}^* + ... \tag{8}$$

$$\mathbf{Q} = 2(\mathbf{E} + \mathbf{E}_s)\cdot\mathbf{A}^* + ... \tag{9}$$

$$\mathbf{E}_{\mathrm{rad},t} = \mathbf{E}^{(E1)} + \mathbf{E}_s^{(E1)} + \mathbf{E}^{(M1)} + \mathbf{E}_s^{(M1)} + \mathbf{E}^{(E2)} + \mathbf{E}_s^{(E2)}... \tag{10}$$

$$\mathbf{B}_{\mathrm{rad},t} = \mathbf{B}^{(E1)} + \mathbf{B}_s^{(E1)} + \mathbf{B}^{(M1)} + \mathbf{B}_s^{(M1)} + \mathbf{B}^{(E2)} + \mathbf{B}_s^{(E2)}... \tag{11}$$

Similarly to eq 4, the Poynting vector is then calculated as $\mathbf{S} = Re(\mathbf{E}_{\mathrm{rad},t} \times \mathbf{B}^*_{\mathrm{rad},t})/2\mu_0$. Out of this expression, there will be leading terms that can again be identified as $\alpha\alpha$, αG, and αA. Their coefficients will be different, however.

In terms of the electromagnetic picture, there are two related types of enhancement mechanisms. First, the induced multipole moments are increased due to the addition of strong scattered local fields and gradients. The radiating fields are increased by this effect and further increased by their own scattering from the nanoparticle. Within the electric dipole approximation for SERS, it turns out that the enhancement is roughly a product of factors that are the same function of frequency except evaluated at different (laser and Raman-shifted) frequencies.[22] When more molecular multipoles are included, they may each exhibit their own enhancement curves, and it becomes necessary to develop further extensions of the KWC vector spherical harmonic field calculations.

III. Plane Wave Scattering

The three-component functions used for solution of the vector Helmholtz equation with spherical symmetry are $\mathbf{L}^z_{\sigma lm}$, $\mathbf{M}^z_{\sigma lm}$, and $\mathbf{N}^z_{\sigma lm}$. The $\mathbf{L}^z_{\sigma lm}$ are not required for a solenoidal (divergenceless) electromagnetic field.[28,36,37] In spherical coordinates r, θ, and ϕ, the other functions are

$$\mathbf{M}^z_{\sigma lm}(k\mathbf{r}) = \hat{\theta} m z_l(kr)\frac{P_l^m(\cos\theta)}{\sin\theta}\begin{pmatrix}-\sin m\phi\\ \cos m\phi\end{pmatrix} - \hat{\phi} z_l(kr)\frac{dP_l^m(\cos\theta)}{d\theta}\begin{pmatrix}\cos m\phi\\ \sin m\phi\end{pmatrix} \tag{12}$$

$$\mathbf{N}^z_{\sigma lm}(k\mathbf{r}) = \hat{r} l(l+1)\frac{z_l(kr)}{kr}P_l^m(\cos\theta)\begin{pmatrix}\cos m\phi\\ \sin m\phi\end{pmatrix} + \hat{\theta}\eta_l^z(kr)\frac{dP_l^m(\cos\theta)}{d\theta}\begin{pmatrix}\cos m\phi\\ \sin m\phi\end{pmatrix} + \hat{\phi} m\eta_l^z(kr)\frac{P_l^m(\cos\theta)}{\sin\theta}\begin{pmatrix}-\sin m\phi\\ \cos m\phi\end{pmatrix} \tag{13}$$

The index $\sigma = e$ or o, according to whether, respectively, the upper or lower function of ϕ is used. The associated Legendre polynomials $P_l^m(\cos\theta)$ are chosen with the Condon-Shortley phase choice. The superscript $z = j$ if $z_l(kr) = j_l(kr)$ and h if $z_l(kr) = h_l^{(1)}(kr)$, corresponding to spherical Bessel functions regular at the origin and to outgoing spherical Hankel functions, respectively. The remaining radial functions are $\eta_l^z(x) = [xz_l(x)]'/x$, where the prime indicates differentiation with respect to x.

Let us assume that a CW laser field $\mathbf{E}$ with frequency ω_0, wavenumber k_0 and wavelength λ_0 is incident on a nanosphere centered on the origin. If the surrounding medium has refractive index n, then $\omega_0 = k_0c/n = 2\pi c/n\lambda_0$. Specifying that $\mathbf{E}$ corresponds to $e^{-i\omega_0 t}$ time-dependence, propagation is along the z-axis and polarization is along the x-axis, then[28]

$$\mathbf{E}(\mathbf{r}) = E_0\hat{x}e^{ik_0z} = E_0\sum_{l=1}^{\infty} i^{l+2}\frac{2l+1}{l(l+1)}[\mathbf{M}^j_{ol1}(k_0\mathbf{r}) - i\mathbf{N}^j_{el1}(k_0\mathbf{r})] \tag{14}$$

Similar expansions hold for internal nanoparticle fields and scattered external fields, all of which must be matched at the particle surface. For the scattered field, this leads to

$$\mathbf{E}_s(\mathbf{r}) = E_0\sum_{l=1}^{\infty} i^{l+2}\frac{2l+1}{l(l+1)}[a_l(\omega_0)\mathbf{M}^h_{ol1}(k_0\mathbf{r}) - ib_l(\omega_0)\mathbf{N}^h_{el1}(k_0\mathbf{r})] \tag{15}$$

where $a_l(\omega_0)$ and $b_l(\omega_0)$ are well-known Mie coefficients involving the permittivities of the nanosphere and the medium.[27,36,37] The expansions for other initial polarizations (e.g., along the y-axis) will also involve the other vector functions $\mathbf{M}^z_{el1}(k_0\mathbf{r})$ and $\mathbf{N}^z_{ol1}(k_0\mathbf{r})$.

If the nanoparticle is instead a metal nanoshell with a dielectric material core, the complete solution requires coefficient matching at both inner and outer surfaces using different expansions in each region. However, the expansion basis in the external region is the same as for a nanosphere, and only the explicit forms for the Mie coefficients a_l and b_l differ.[31] For scattering with molecules external to the nanoparticle, it is only

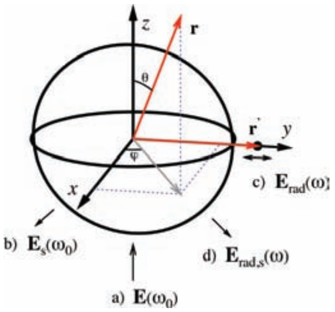

Figure 1. Molecule at position $\mathbf{r}'$ outside a metal nanoparticle centered at the origin is exposed to (a) an external plane-wave field and (b) its wave scattered from the particle, both at frequency ω_0. Molecular multipole moments are then induced corresponding to (c) a field radiating from the molecule and (d) a secondary field scattered from the particle, both at Raman-shifted frequency ω. Both (c) and (d) can be broken into $E1$, $M1$, and $E2$ parts.

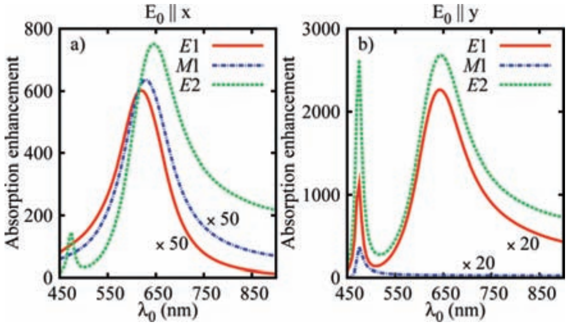

Figure 2. Enhancement factors for incident fields involved in absorption by a 40/50 nm silver nanoshell. Here $|\mathbf{E} + \mathbf{E}_s|^2/|\mathbf{E}|^2$, $|\mathbf{B} + \mathbf{B}_s|^2/|\mathbf{B}|^2$ and $|\nabla\mathbf{E} + \nabla\mathbf{E}_s|^2/|\nabla\mathbf{E}|^2$ are shown to each have their own enhancement curves as functions of wavelength and of initial polarization. The incident electric field $\mathbf{E}$ is along the x axis in (a) and along the y axis in (b). Fields are evaluated at the molecular position $\mathbf{r}'$ 1 nm outside the nanoshell along the y axis.

this external field that is needed. In everything that follows we use the more versatile nanoshell geometry with its tunable surface plasmons for purposes of generality, and solid nanospheres are regarded as the special case where the dielectric core vanishes.

In the Mie theory literature, the nanoparticle field contributions for $l = 1, 2, 3, \ldots$ are called dipole, quadrupole, octupole, ... terms, respectively. These are not to be confused with the *molecular* multipole moments of the same names that are the focus here. Nevertheless, all nanoparticle-multipole terms, as well as all orders of retardation (i.e., effects due to the finite speed of light), are included in the calculations.

The other expansions required in eq 7 are the magnetic field $\mathbf{B}$ and the outer product $\nabla\mathbf{E}$ (a two-dimensional tensor). The $\mathbf{B}$ expansion is easily obtained by using $i\omega_0\mathbf{B} = \nabla \times \mathbf{E}$ and the curl equations $\nabla \times \mathbf{M}^z_{\sigma lm} = k_0\mathbf{N}^z_{\sigma lm}$ and $\nabla \times \mathbf{N}^z_{\sigma lm} = k_0\mathbf{M}^z_{\sigma lm}$.[36] The $\nabla\mathbf{E}$ expansion has also been implemented in spherical coordinates, though these terms need to be grouped carefully so that apparent singularities at $\theta = 0$ and π cancel properly, and is converted to Cartesian coordinates as needed. All expansions have been implemented within Mathematica.

An example is shown schematically in Figure 1, where a molecule lies on the y axis outside a spherical metal particle. The incident plane wave field $\mathbf{E}$ and the scattered field $\mathbf{E}_s$ both coexist outside the particle, as do their magnetic field and gradient field counterparts (not indicated). Focusing on the induced electric dipole of eq 7 in the electric dipole approximation, the magnitude of $\mathbf{d}$ is determined by $\mathbf{E} + \mathbf{E}_s$ at the position $\mathbf{r}'$ of the molecule. As a general measure of the transition intensity, independent of the specific choice of polarizability tensor, the quantity $|\mathbf{E} + \mathbf{E}_s|^2/|\mathbf{E}|^2$ is shown as a function of wavelength for a 40/50 nm (inner/outer radius) silver nanoshell in Figure 2 for two different initial polarizations and for the molecule outside the outer shell surface. Also shown are $|\mathbf{B} + \mathbf{B}_s|^2/|\mathbf{B}|^2$ and $|\nabla\mathbf{E} + \nabla\mathbf{E}_s|^2/|\nabla\mathbf{E}|^2$, where the latter square norm is a summation over the absolute-squares of the components of the gradient tensor. These represent generalized enhancement plots for the different pure-multipole absorption transitions.

The broader long-wavelength resonance features in Figure 2 correspond to $l = 1$ (nanoparticle-dipole) contributions in eqs 14 and 15, while the narrower short-wavelength features correspond to $l = 2$ (nanoparticle-quadrupole). It is seen that these enhancements are generally greater for polarization in the direction of the molecule (y polarization here), and that the molecular $E2$ enhancements are the strongest. The $M1$ enhancements are the smallest, though they can be comparable to the $E1$ enhancements in some cases. These conclusions continue to hold upon examining other geometries and polarizations. The dynamic variation of the local fields is sufficiently strong that the electric field gradient, and hence the $E2$ response tensor $\mathbf{A}$, becomes a more significant contributor to scattering than in the absence of the nanoparticle [cf., eq 7].

The symmetries of the $l = 1$ dipole modes allow for stronger interaction with incident light, so one may in general terms expect their resonant contributions to be both greater and broader compared to $l = 2$. In Mie theory, the resonant behavior may be easily examined in the nonretarded limit where only the leading small-argument terms from the spherical Bessel functions are used. One finds in this limit that the resonant behavior in the 40/50 Ag nanoshell Mie coefficients is encountered at wavelengths λ for which the Ag permittivity obeys $Re(\varepsilon) \sim -7$ for $l = 1$ and ~ -13 for $l = 2$. From the Johnson and Christie dielectric data, this leads to values of $Im(\varepsilon)$ for the $l = 1$ resonance that are over twice as large as those for $l = 2$, partially explaining the greater dipole spectral width. However, if one uses the exact Mie scattering coefficients, it is found that the dipole plasmon response undergoes much more significant red-shifting and broadening than the quadrupole response. Thus, retardation effects also contribute to the different $l = 1$ and 2 behaviors.

For the αG and αA terms, this examination is only half the story. There are similar cross-terms whether it is the absorption step or the emission step that is $E1$, and we have so far only discussed the case corresponding to $E1$ emission. Equations 8 and 9 are pertinent to establishing $M1$ and $E2$ radiating fields due to $E1$ absorption. Will the resulting cross-terms have similar enhancement curves in these separate cases? The direct way to answer this requires evaluation of these higher multipole fields, the task to which we turn next.

IV. Multipole Field Scattering

A. Field Expansions from the Dyadic Green Tensor. The classical EM fields observed at $\mathbf{r}$ due to multipole moments at $\mathbf{r}'$ may be derived by using the dyadic electromagnetic Green tensor (a 2D tensor formed from outer products of 1D vectors)[22,29,30]

$$\mathbf{G}(k, \mathbf{r}, \mathbf{r}') = \frac{ik}{\pi} \sum_{\sigma=e}^{o} \sum_{l=1}^{\infty} \sum_{m=0}^{l} D_{lm}[\mathbf{M}^{z}_{\sigma lm}(k\mathbf{r})\mathbf{M}^{z'}_{\sigma lm}(k\mathbf{r}') + \mathbf{N}^{z}_{\sigma lm}(k\mathbf{r})\mathbf{N}^{z'}_{\sigma lm}(k\mathbf{r}')] \quad (16)$$

$$D_{lm} = (2 - \delta_{m0})\frac{2l + 1}{4l(l + 1)}\frac{(l - m)!}{(l + m)!} \quad (17)$$

where $\{z, z'\} = \{h, j\}$ for $r > r'$ and $\{j, h\}$ for $r < r'$.

The free-space electric permittivity ε_0 and magnetic permeability μ_0 satisfy $\sqrt{(\varepsilon_0\mu_0)} = 1/c$. The corresponding quantities in a general material are taken to be $\varepsilon\varepsilon_0$ and $\mu\mu_0$, where the relative permittivity ε and permeability μ satisfy $\sqrt{(\varepsilon\mu)} = kc/\omega = n$, with k the wavenumber and n the index of refraction at the Raman-shifted frequency $\omega = kc/n = 2\pi c/n\lambda$. The index of refraction is generally complex for absorbing materials. Only nonmagnetic materials ($\mu = 1$) are considered below.

As described by Ben-Menahem,[29] in the vector potential

$$\mathbf{A}(\mathbf{r}) = \mu\mu_0 \int \mathbf{G}(k, \mathbf{r}, \mathbf{r}')\cdot\mathbf{J}(\mathbf{r}')\, \mathrm{d}\mathbf{r}' \quad (18)$$

the current $\mathbf{J}$ arises from localized charges moving within a small molecular volume centered around $\mathbf{r}'$. For $\mathbf{s}$ considered as a small displacement from $\mathbf{r}'$, one may expand $\mathbf{G}$ as

$$\mathbf{G}(k, \mathbf{r}, \mathbf{r}' + \mathbf{s}) = \mathbf{G}(k, \mathbf{r}, \mathbf{r}') + \mathbf{s}\cdot\nabla'\mathbf{G}(k, \mathbf{r}, \mathbf{r}') + ... \quad (19)$$

and convert the $\mathbf{r}'$ integration to one over $\mathbf{s}$. Using manipulations as described by Jackson,[34] one finally arrives at

$$\mathbf{E}_{\mathrm{rad}}(\mathbf{r}) = \frac{k^2c^2\mu\mu_0}{n^2}\mathbf{G}(k, \mathbf{r}, \mathbf{r}')\cdot\mathbf{d} + \frac{ikc\mu\mu_0}{n}[\mathbf{m}\cdot\nabla' \times \mathbf{G}^T(k, \mathbf{r}, \mathbf{r}')]^T + \frac{k^2c^2\mu\mu_0}{6n^2}[\nabla'\cdot\mathbf{Q}\cdot\mathbf{G}^T(k, \mathbf{r}, \mathbf{r}')]^T + ... \quad (20)$$

The molecular multipole moments with $\mathbf{r}'$ as origin are (ρ is the charge density)

$$\mathbf{d} = \int \mathbf{s}\rho(\mathbf{s})\, \mathrm{d}\mathbf{s} \quad (21)$$

$$\mathbf{m} = \frac{1}{2}\int \mathbf{s} \times \mathbf{J}(\mathbf{s})\, \mathrm{d}\mathbf{s} \quad (22)$$

$$Q_{\alpha\beta} = \int (3s_\alpha s_\beta - s^2\delta_{\alpha\beta})\rho(\mathbf{s})\, \mathrm{d}\mathbf{s} \quad (23)$$

The quadrupole tensor here is traceless and symmetric. The use of multiple transposes in eq 20 is just a device to temporarily bring the $\mathbf{r}'$ indices of $\mathbf{G}$ to the left before differentiation. Alternatively, one can write, for example, $(\nabla'\cdot\mathbf{Q}\cdot\mathbf{G}^T)^T = (\mathbf{G}\overleftarrow{\nabla}')$: $\mathbf{Q}$, using left-differentiation, double tensor contraction and the symmetry of $\mathbf{Q}$. This latter form will be useful later.

The first electric field we encounter then corresponds to a classical electric dipole radiating at the Raman-shifted frequency

$$\mathbf{E}^{(E1)}(\mathbf{r}) = \frac{k^2c^2\mu\mu_0}{n^2}\mathbf{G}(k, \mathbf{r}, \mathbf{r}')\cdot\mathbf{d} = \frac{ik^3}{\pi\varepsilon\varepsilon_0} \sum_{\sigma=e}^{o} \sum_{l=1}^{\infty} \sum_{m=0}^{l} D_{lm}\{\mathbf{M}^{z}_{\sigma lm}(k\mathbf{r})[\mathbf{M}^{z'}_{\sigma lm}(k\mathbf{r}')\cdot\mathbf{d}] + \mathbf{N}^{z}_{\sigma lm}(k\mathbf{r})[\mathbf{N}^{z'}_{\sigma lm}(k\mathbf{r}')\cdot\mathbf{d}]\} \quad (24)$$

This result is precisely as obtained by KWC[22] and includes contributions from general m, unlike the plane wave expansion. The choice of spherical Bessel and Hankel functions z and z' depend on the coordinate regions examined.

The $M1$ contribution to the radiating electric field may be derived almost as easily by using the curl equations for the $\mathbf{M}$ and $\mathbf{N}$ functions mentioned above, in this case using k instead of k_0. The result is similar to the $E1$ contribution but with $\mathbf{d} \rightarrow \mathbf{m}$ and interchange of the $\mathbf{M}$ and $\mathbf{N}$ functions containing argument $\mathbf{r}'$

$$\mathbf{E}^{(M1)}(\mathbf{r}) = -\frac{k^3c\mu\mu_0}{\pi n} \sum_{\sigma=e}^{o} \sum_{l=1}^{\infty} \sum_{m=0}^{l} D_{lm}\{\mathbf{M}^{z}_{\sigma lm}(k\mathbf{r})[\mathbf{N}^{z'}_{\sigma lm}(k\mathbf{r}')\cdot\mathbf{m}] + \mathbf{N}^{z}_{\sigma lm}(k\mathbf{r})[\mathbf{M}^{z'}_{\sigma lm}(k\mathbf{r}')\cdot\mathbf{m}]\} \quad (25)$$

The $E2$ contribution is more difficult and depends on the parametrization chosen for the electric quadrupole tensor. We choose the five independent quantities defining this traceless tensor as $Q_\pm = (Q_{xx} \pm Q_{yy})/2$, Q_{xy}, Q_{xz}, and Q_{yz}. Then the operator $\nabla'\cdot\mathbf{Q}$ in eq 20 is a row vector

$$\nabla'\cdot\mathbf{Q} = \Big[(Q_+ + Q_-)\frac{\partial}{\partial x'} + Q_{xy}\frac{\partial}{\partial y'} + Q_{xz}\frac{\partial}{\partial z'}, Q_{xy}\frac{\partial}{\partial x'} + (Q_+ - Q_-)\frac{\partial}{\partial y'} + Q_{yz}\frac{\partial}{\partial z'}, Q_{xz}\frac{\partial}{\partial x'} + Q_{yz}\frac{\partial}{\partial y'} - 2Q_+\frac{\partial}{\partial z'}\Big] \quad (26)$$

The electric field component arising from excitation via the $E2$ molecular moment thereby becomes

$$\mathbf{E}^{(E2)}(\mathbf{r}) = \frac{ik^3}{6\pi\varepsilon\varepsilon_0} \sum_{\sigma=e}^{o} \sum_{l=1}^{\infty} \sum_{m=0}^{l} D_{lm}\{\mathbf{M}^{z}_{\sigma lm}(k\mathbf{r})[\nabla'\cdot\mathbf{Q}\cdot\mathbf{M}^{z'}_{\sigma lm}(k\mathbf{r}')] + \mathbf{N}^{z}_{\sigma lm}(k\mathbf{r})[\nabla'\cdot\mathbf{Q}\cdot\mathbf{N}^{z'}_{\sigma lm}(k\mathbf{r}')]\} \quad (27)$$

The coefficients in square brackets have been explicitly evaluated by converting to spherical coordinates and using eqs 12 and 13, though they are lengthy and not included here.

Each of the primary molecular multipole fields produces a field scattered from the nanoparticle, so that the total fields at the Raman-shifted frequency are each a sum of primary and scattered contributions, e.g., $\mathbf{E}_t^{(E1)}(\mathbf{r}) = \mathbf{E}^{(E1)}(\mathbf{r}) + \mathbf{E}_s^{(E1)}(\mathbf{r})$. To determine the scattered fields, one may match tangential electric and magnetic field components at the shell boundaries in Mie-type calculations. For determination of the radiation in the far zone, we are interested in the region $r > r'$. The total $E1$ electric field there is given by

$$\mathbf{E}_t^{(E1)}(\mathbf{r}) = \frac{ik^3}{\pi\varepsilon\varepsilon_0}\sum_{\sigma=e}^{o}\sum_{l=1}^{\infty}\sum_{m=0}^{l} D_{lm}[\mathbf{M}^h_{\sigma lm}(k\mathbf{r})f^{(E1,t)}_{\sigma lm} + \mathbf{N}^h_{\sigma lm}(k\mathbf{r})g^{(E1,t)}_{\sigma lm}] \quad (28)$$

$$f^{(E1,t)}_{\sigma lm} = \mathbf{M}^j_{\sigma lm}(k\mathbf{r}')\cdot\mathbf{d} + a_l(\omega)\mathbf{M}^h_{\sigma lm}(k\mathbf{r}')\cdot\mathbf{d} \quad (29)$$

$$g^{(E1,t)}_{\sigma lm} = \mathbf{N}^j_{\sigma lm}(k\mathbf{r}')\cdot\mathbf{d} + b_l(\omega)\mathbf{N}^h_{\sigma lm}(k\mathbf{r}')\cdot\mathbf{d} \quad (30)$$

The $a_l(\omega)$ and $b_l(\omega)$ coefficients are precisely the same Mie coefficients as in eq 15 but evaluated at the Raman-shifted frequency ω. Of special note is the fact that they are not dependent on m. Similarly, the total $M1$ electric field is

$$\mathbf{E}_t^{(M1)}(\mathbf{r}) = -\frac{k^3 c\mu\mu_0}{\pi n}\sum_{\sigma=e}^{o}\sum_{l=1}^{\infty}\sum_{m=0}^{l} D_{lm}[\mathbf{N}^h_{\sigma lm}(k\mathbf{r})f^{(M1,t)}_{\sigma lm} + \mathbf{M}^h_{\sigma lm}(k\mathbf{r})g^{(M1,t)}_{\sigma lm}] \quad (31)$$

$$f^{(M1,t)}_{\sigma lm} = \mathbf{M}^j_{\sigma lm}(k\mathbf{r}')\cdot\mathbf{m} + b_l(\omega)\mathbf{M}^h_{\sigma lm}(k\mathbf{r}')\cdot\mathbf{m} \quad (32)$$

$$g^{(M1,t)}_{\sigma lm} = \mathbf{N}^j_{\sigma lm}(k\mathbf{r}')\cdot\mathbf{m} + a_l(\omega)\mathbf{N}^h_{\sigma lm}(k\mathbf{r}')\cdot\mathbf{m} \quad (33)$$

and the total $E2$ electric field is

$$\mathbf{E}_t^{(E2)}(\mathbf{r}) = \frac{ik^3}{6\pi\varepsilon\varepsilon_0}\sum_{\sigma=e}^{o}\sum_{l=1}^{\infty}\sum_{m=0}^{l} D_{lm}[\mathbf{M}^h_{\sigma lm}(k\mathbf{r})f^{(E2,t)}_{\sigma lm} + \mathbf{N}^h_{\sigma lm}(k\mathbf{r})g^{(E2,t)}_{\sigma lm}] \quad (34)$$

$$f^{(E2,t)}_{\sigma lm} = \nabla'\cdot\mathbf{Q}\cdot\mathbf{M}^j_{\sigma lm}(k\mathbf{r}') + a_l(\omega)\nabla'\cdot\mathbf{Q}\cdot\mathbf{M}^h_{\sigma lm}(k\mathbf{r}') \quad (35)$$

$$g^{(E2,t)}_{\sigma lm} = \nabla'\cdot\mathbf{Q}\cdot\mathbf{N}^j_{\sigma lm}(k\mathbf{r}') + b_l(\omega)\nabla'\cdot\mathbf{Q}\cdot\mathbf{N}^h_{\sigma lm}(k\mathbf{r}') \quad (36)$$

The corresponding magnetic fields can again be obtained using $i\omega\mathbf{B} = \nabla \times \mathbf{E}$ and the curl equations between the **M**'s and **N**'s. This affects only the functions of argument (k**r**), leaving the f and g coefficients unchanged. The significance of the above results is that the scattered version of each multipole field can be evaluated in terms of known vector functions (or operations thereon) and Mie-type coefficients $a_l(\omega)$ and $b_l(\omega)$ that are *precisely* the same as those arising in the plane wave expansion except evaluated at a different frequency. There are no other unknowns. This result in the $E1$ case was discussed for spheres by KWC, but is seen to be more general.

For some scattering geometries, e.g., input field propagation along the z-axis, polarization vector and molecule along the y-axis, and observation along the x-axis, KWC point out that the $E1$ results of eqs 28-30 reduce to simple expressions. For more general geometries, especially for increasing kr or kr', convergence can be excruciatingly slow. It turns out that the m and σ sums can be evaluated in closed form for each of the total multipole fields using the spherical harmonic addition theorem as well as the m- and σ-independence of the scattering coefficients. This has been exploited in the calculations.

B. Spatial Patterns of Multipole Fields. We evaluate in Figures 3−5 the magnitudes of the field components for a molecule located on the y-axis ($\theta' = \phi' = \pi/2$) exactly 1 nm outside the 40/50 silver nanoshell ($r' = 51$ nm). For observation radius $r = 55$ nm, the close proximity causes the primary+scattered fields from each of the molecular multipoles to be highly peaked over a narrow range of θ and ϕ values in the neighborhood of $\pi/2$. The radiation wavelength is taken as 620 nm in this example.

To illustrate, Figure 3 shows surface plots of the $\mathbf{E}_t^{(E1)}$ field amplitudes for the classical electric dipole. In general, the electric dipole can be expressed in spherical coordinates, $\mathbf{d} = d_r\hat{r} + d_\theta\hat{\theta} + d_\phi\hat{\phi}$. We calculate $\mathbf{E}_t^{(E1)}$ at the Raman-scattered frequency ω separately in the three cases $\mathbf{d} = \hat{r}$, $\hat{\theta}$, and $\hat{\phi}$. Thus the first row of Figure 3 shows the magnitudes $|\mathbf{E}_r^{(E1)}|$, $|\mathbf{E}_\theta^{(E1)}|$, and $|\mathbf{E}_\phi^{(E1)}|$ for a radial electric dipole $\mathbf{d} = \hat{r}$, while the next two rows show the same components when $\mathbf{d} = \hat{\theta}$ and $\mathbf{d} = \hat{\phi}$, respectively. One sees approximate symmetry across the diagonal, e.g., $\hat{r}\hat{\theta}$ versus $\hat{\theta}\hat{r}$, which is ascribed to symmetries in the dyadic Green Tensor. The maximum field is attained when both the dipole and the observation point are in the radial (y) direction. For general electric dipoles, one may add the (complex) response components together by linear superposition.

Figure 4 shows the corresponding $M1$ field component magnitudes (columns) due to classical unit magnetic dipoles along spherical axes (rows). In this case the responses are transverse to the sources, exactly zero for the $\hat{r}\hat{r}$ panel and very small for the $\hat{\theta}\hat{\theta}$ and $\hat{\phi}\hat{\phi}$ panels. (There is a symmetry here; this is the behavior we would also expect for $\mathbf{B}^{(E1)}$.) Maximum responses are obtained for the $\hat{\theta}\hat{\phi}$ and $\hat{\phi}\hat{\theta}$ cases. Figure 5 shows the $E2$ field component magnitudes generated by the individual electric quadrupole components Q_+, Q_-, Q_{xy}, Q_{xz}, and Q_{yz}, each in turn being taken to have unit magnitude while the others are zero.

The signal obtained at the remote detector location (r, θ, ϕ), $kr \gg 1$, is proportional to $|\mathbf{F}(\theta,\phi)|^2$, where

$$\mathbf{F}(\theta, \varphi) = [r\mathrm{e}^{-ikr}\mathbf{E}_{\mathrm{rad},t}(r, \theta, \phi)]_{kr\to\infty} \quad (37)$$

The latter is a superposition of contributions from the different multipole fields and is evaluated using known asymptotic forms for the spherical Bessel functions. (The asymptotic components are not as angularly confined as the near-field versions shown in Figures 3−5.) One may calculate enhancements of radiated intensity in specific directions as done by KWC for $E1$-only emission, calculating $\mathbf{F}(\theta,\phi)$ in both the presence and absence of the nanoparticle. This ratio can of course be singular in directions for which the unenhanced $\mathbf{F}(\theta,\phi)$ vanishes, so we seek nonsingular characteristic measures of the enhancements each type of radiation field can produce.

To this end, the sums of the $|F_x|^2$ arising from the three different (unit) dipole components in the $E1$ and $M1$ cases and the five different (unit) quadrupole components in the $E2$ case are calculated, both with and without the nanoparticle present. The ratio of enhanced to unenhanced sums for the three types of fields are shown in Figure 6 for the 40/50 Ag nanoshell as a function of emission wavelength. It is clear that the peak enhancements follow the same general pattern as the average absorption-step enhancements (Figure 2b in particular): $M1 < E1 \ll E2$, with similar orders of magnitude. Thus, quite generally, αA cross-terms may gain in significance relative to αG terms in the case of SEROA. In ROA, the αG cross-terms tend to dominate (see Luber et al. and references therein[35]), but this need not be the case in SEROA.

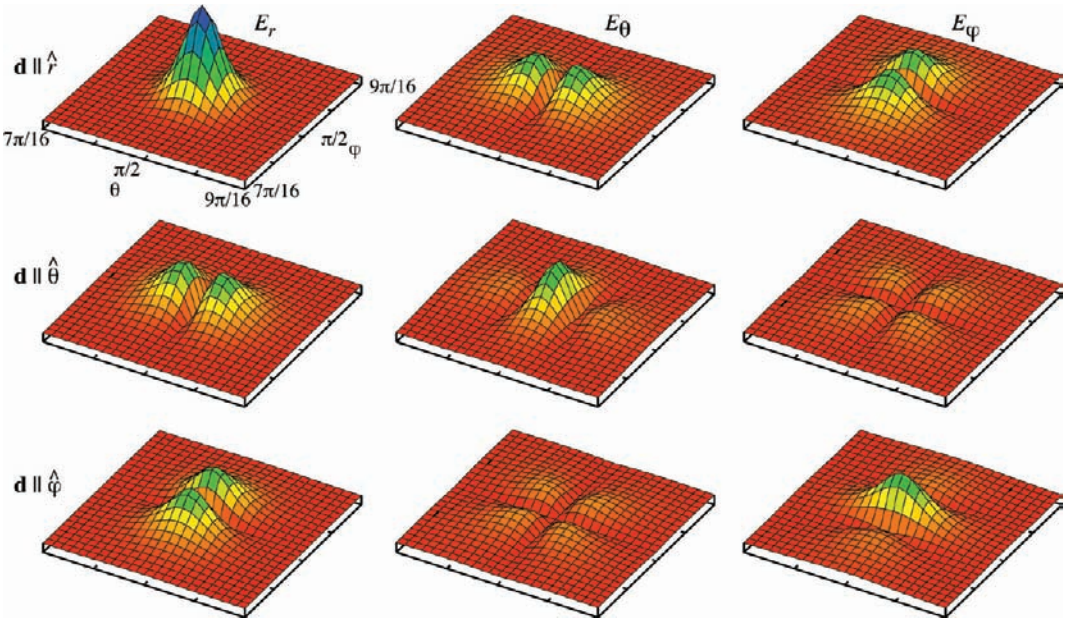

Figure 3. Plots of $|E_r^{(E1)}|$, $|E_\theta^{(E1)}|$, and $|E_\phi^{(E1)}|$ (columns 1, 2, and 3, respectively) arising from unit electric dipoles $\mathbf{d} = \hat{r}$, $\hat{\theta}$, and $\hat{\phi}$ (rows 1, 2, and 3, respectively).

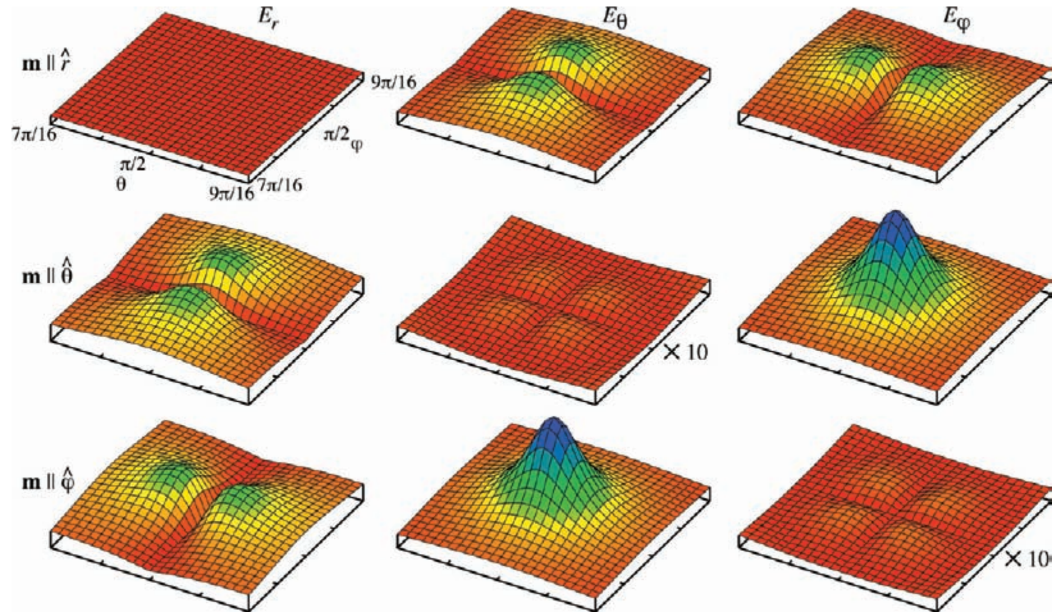

Figure 4. Plots of $|E_r^{(M1)}|$, $|E_\theta^{(M1)}|$, and $|E_\phi^{(M1)}|$ (columns 1, 2, and 3, respectively) arising from unit magnetic dipoles $\mathbf{m} = \hat{r}$, $\hat{\theta}$, and $\hat{\phi}$ (rows 1, 2, and 3, respectively).

In a different context, absorption rates for electric dipole and quadrupole transitions have been compared for idealized spherical GaAs quantum dots by Zurita-Sánchez and Novotny.[38] In the near field of a metal tip exposed to plane-wave excitation, the strong local variation of the field can lead to $E2$ rates only slightly less than $E1$ rates, whereas far-field $E2$ excitation is some 3 orders of magnitude lower. (Near-zone $M1$ transition rates can also exceed $E1$ transition rates under special circumstances for quantum dots[39] but not for atoms or molecules.) It is reasonable in general that near-field phenomena can be marked by increased importance of electric quadrupole contributions.

V. Application to a Chiral Molecule Model

We wish to obtain SEROA enhancement profiles throughout the visible/NIR spectrum incorporating both absorption and emission enhancements, similar to the SERS enhancement profiles calculated by KWC (their Figure 2). Besides including higher multipoles, however, we also want to include wavelength dependence of the molecular response tensors and we want the latter to be the "derived" response tensors appropriate for Raman transitions. For example, according to Placzek theory,[7,40,41] the correct polarizability tensor to use for vibrational scattering between initial υ^i and final υ^f vibrational levels is $\langle \upsilon^f | \boldsymbol{\alpha} | \upsilon^i \rangle$, where $\boldsymbol{\alpha}$ may be Taylor-expanded about the equilibrium molecular geometry to give

$$\langle \upsilon^f | \alpha_{kl} | \upsilon^i \rangle = (\alpha_{kl})_e \delta_{\upsilon^f \upsilon^i} + \sum_j (\partial \alpha_{kl} / \partial Q_j)_e \langle \upsilon^f | Q_j | \upsilon^i \rangle + ... \quad (38)$$

The first term corresponds to Rayleigh scattering while the next terms correspond in the harmonic approximation to the various

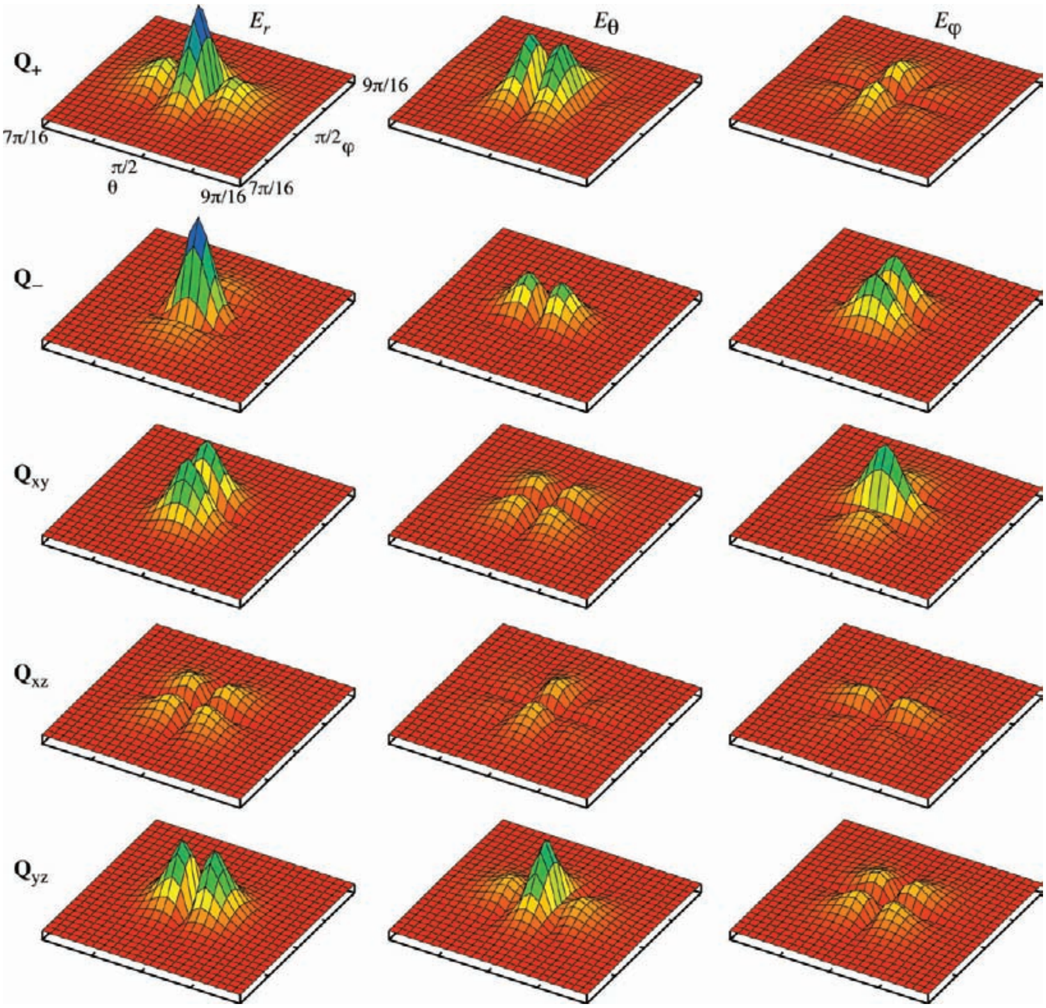

Figure 5. Plots of $|E_r^{(E2)}|$, $|E_\theta^{(E2)}|$, and $|E_\phi^{(E2)}|$ (columns 1, 2, and 3, respectively) arising from unit electric quadrupole moments Q_+, Q_-, Q_{xy}, Q_{xz}, and Q_{yz} (rows 1−5, respectively).

Raman fundamental modes. Similarly the **G′** and **A** tensors can be Taylor-expanded[7] and their first derivatives calculated with respect to the normal coordinate Q_j of interest. For a fundamental transition in mode j in the harmonic approximation, the quantum sum-over-states formulas for the derived response tensors are[32]

$$\frac{\partial \alpha_{kl}}{\partial Q_j} = \frac{2}{\hbar}\frac{\partial}{\partial Q_j}\sum_{n\neq 1}\frac{\omega_{n1}}{\omega_{n1}^2 - \omega^2}Re[\langle 1|\hat{d}_k|n\rangle\langle n|\hat{d}_l|1\rangle] \tag{39}$$

$$\frac{\partial G'_{kl}}{\partial Q_j} = -\frac{2}{\hbar}\frac{\partial}{\partial Q_j}\sum_{n\neq 1}\frac{\omega}{\omega_{n1}^2 - \omega^2}Im[\langle 1|\hat{d}_k|n\rangle\langle n|\hat{m}_l|1\rangle] \tag{40}$$

$$\frac{\partial A_{ikl}}{\partial Q_j} = \frac{1}{\hbar}\frac{\partial}{\partial Q_j}\sum_{n\neq 1}\frac{\omega_{n1}}{\omega_{n1}^2 - \omega^2}Re[\langle 1|\hat{d}_i|n\rangle\langle n|\hat{Q}_{kl}|1\rangle] \tag{41}$$

Within the Born−Oppenheimer separation, both energies and transition matrix elements depend on the normal coordinates.

While there is progress being made in the ab initio calculation of such quantities,[35,42−44] it is more useful for our current purposes to adopt the qualitative twisted-arc model, which has been applied by Trost and Hornberger[23] to hydrogen persulfide, H_2S_2 (Figure 7), a small molecule forming enantiomeric pairs. The simple 1D twisted-arc model considers a delocalized electron to move within a "box" formed from two planar arcs joined at the center of H_2S_2 and twisted with respect to each other by the dihedral angle χ. Trost and Hornberger derive quantum mechanical wave functions and matrix elements exhibiting simple χ dependences, allowing sum-over-states evaluation of ROA tensors that can easily be differentiated with respect to χ. Thus we can obtain derived ROA tensors depending both on the excitation frequency (dynamical tensors) and on the particular vibrational coordinate that controls the chirality of the molecule. Ignoring coupling to other coordinates, χ is approximately the torsional normal coordinate Q_4 of H_2S_2, which has wavenumber[45] $\tilde{\nu}_4 \sim 420$ cm^{-1} and a diagonal harmonic force constant[46] $f_{44} \sim 0.092$ aJ/rad^2.

Avoiding notational clutter, we continue to use the **α**, **G′**, and **A** symbols below, though in actuality their derivatives with respect to χ are used. Issues of reactivity are ignored as this is a spectroscopic model that will be augmented only by plasmonic enhancement effects. The first excited electronic state is in the UV region of the spectrum, so the Raman scattering we calculate is effectively far-from-resonance.

For H_2S_2 molecules near the nanoparticle surface, it is appropriate to average over rotations of the molecules. This is usually performed for plane-wave excitation,[7] but there are

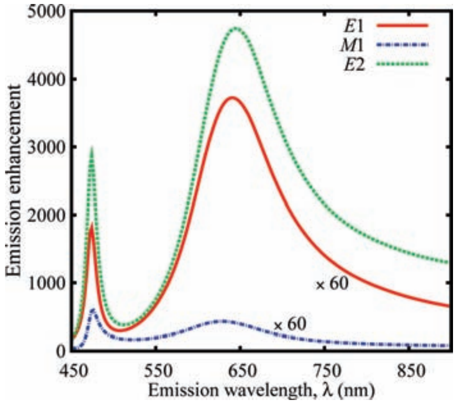

Figure 6. Asymptotic emission enhancement (averaged as explained in the text) along the *x* axis for different induced multipoles in a molecule outside a 40/50 Ag nanoshell as functions of radiating wavelength.

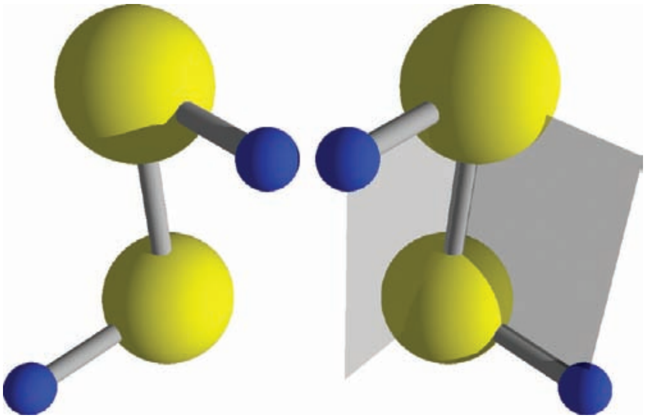

Figure 7. Enantiomers of H_2S_2.

differences due to the plasmonic local fields. We may write the total radiative electric field as

$$\mathbf{E}_{\mathrm{rad},t} = \mathbf{T}^{(E1)}\cdot\mathbf{d} + \mathbf{T}^{(M1)}\cdot\mathbf{m} + \mathbf{T}^{(E2)}:\mathbf{Q} \qquad (42)$$

where the explicit forms of the **T** tensors can be extracted directly from eqs 28−36. [For the *E*2 contribution, see the remark after eq 23.] As $r \to \infty$, $\mathbf{E}_{\mathrm{rad},t}$ and $\mathbf{B}_{\mathrm{rad},t}$ are perpendicular to $\hat{r}$ and to each other, both are proportional to e^{ikr}/r, and the Poynting vector is radial and $|\mathbf{S}| = |\mathbf{E}_{\mathrm{rad},t}|^2 n/2\mu_0 c$, where $n = 1.33$ is the refractive index of water. Substituting for the induced dipole moments in eq 42 by use of eqs 7-9, we get the components

$$E_{\mathrm{rad},t,\lambda} \approx \sum_{\mu,\nu} T^{(E1)}_{\lambda,\mu}\left(\alpha_{\mu,\nu}E_{t,\nu} - iG'_{\mu,\nu}B_{t,\nu} + \frac{1}{3}\sum_{\rho} A_{\mu,\nu,\rho}\frac{\partial}{\partial r'_{\nu}}E_{t,\rho}\right) + \sum_{\mu,\nu} T^{(M1)}_{\lambda,\mu}(iG'_{\nu,\mu}E_{t,\nu}) + \sum_{\mu,\nu,\rho} T^{(E2)}_{\lambda,\mu,\nu}(2A_{\rho,\mu,\nu}E_{t,\rho}) \qquad (43)$$

in terms of the response tensors and the local fields oscillating at the initial frequency ω_0. As the molecule rotates, so do the response tensors. Averaging the square of eq 43 over orientations, keeping only terms with at least one $\boldsymbol{\alpha}$ factor

$$\begin{aligned}|E_{\mathrm{rad},t,\lambda}|^2 \approx{}& \sum_{\sigma,\tau,\mu,\nu} E_{t,\tau}^{*}T^{(E1)*}_{\lambda,\sigma}T^{(E1)}_{\lambda,\mu}E_{t,\nu}\langle\alpha_{\sigma,\tau}\alpha_{\mu,\nu}\rangle + \\ & 2Re\left\{\sum_{\sigma,\tau\mu,\nu} E_{t,\tau}^{*}T^{(E1)*}_{\lambda,\sigma}\left[\frac{1}{3}T^{(E1)}_{\lambda,\mu}\sum_{\rho}\frac{\partial}{\partial r'_{\nu}}E_{t,\rho}\langle\alpha_{\sigma,\tau}A_{\mu,\nu,\rho}\rangle + 2\sum_{\rho}T^{(E2)}_{\lambda,\mu,\nu}E_{t,\rho}\langle\alpha_{\sigma,\tau}A_{\rho,\mu,\nu}\rangle\right]\right\} + \\ & 2Im\left\{\sum_{\sigma,\tau,\mu,\nu} E_{t,\tau}^{*}T^{(E1)*}_{\lambda,\sigma}[T^{(E1)}_{\lambda,\mu}B_{t,\nu}\langle\alpha_{\sigma,\tau}G'_{\mu,\nu}\rangle - T^{(M1)}_{\lambda,\mu}E_{t,\nu}\langle\alpha_{\sigma,\tau}G'_{\nu,\mu}\rangle]\right\}\end{aligned} \qquad (44)$$

The averages may be evaluated, as usual, by expressing response tensors in terms of the molecule-fixed frame quantities and direction cosine matrix elements, followed by integration over the Euler angles.[32] This expresses intensities in terms of ROA invariants,[32,47] (sums of products of tensor elements that are independent of rotational frame), as also occurs in ordinary ROA.

There are significant differences in the quantities multiplying the invariants in SEROA, however. At the incident frequency, the local fields $\mathbf{E}_t$ and $\mathbf{B}_t$ are not simply plane waves but also contain nanoparticle-scattered contributions. At the Raman-shifted frequency, the **T** tensors carry the information about not only the molecular multipole fields but also the fields the latter produce in scattering from the nanoparticle.

ICP ROA[7] measures differences in Raman intensities for right- and left-handed incident light, while Scattered Circular Polarization (SCP) ROA[48] analyzes differences between right- and left-handed components of the scattered light for linearly polarized or unpolarized incident light. In the far-from-resonance case, one obtains similar information from ICP and SCP, though the latter has advantages in improving experimental measurements.[49,50] For SEROA in the ICP implementation, one would return to eq 43 and convert to circular polarization descriptions of the incident fields. For SEROA in the SCP configuration, one can start from eq 44 and convert the radiative field $\mathbf{E}_{\mathrm{rad},t}$ from Cartesian indices λ to circular polarization indices. Experimental intensities I_{R} and I_{L} will then be proportional to asymptotic Poynting vectors with the appropriate polarizations. The corresponding experimental CIDs are usually expressed as the dimensionless quantity $(I_{\mathrm{R}} - I_{\mathrm{L}})/(I_{\mathrm{R}} + I_{\mathrm{L}})$.

Discussions of possible *E*1/*E*1 contributions to SEROA CIDs have already been made for adsorbed analytes.[10,11,15] Even in the nonadsorbed case examined here, averaging over molecular rotations generally gives unequal αα contributions to I_{R} and I_{L}, unless the nanoparticle is absent (conventional ROA) or the molecule is in particular positions around the nanoparticle. We have examined the αα, α*G*, and α*A* intensities in both 90° and backscatter detection geometries and using both ICP and SCP SEROA. For the backscatter SCP configuration appropriate to the instrument built at Rice,[25] Table 1 demonstrates rotationally averaged right $|\mathbf{F}_{\mathrm{R}}(\pi,0)|^2$ and left $|\mathbf{F}_{\mathrm{L}}(\pi,0)|^2$ values [cf., eq 37], to which the intensities are proportional. Three angular positions of the molecule are chosen around a 40/50 Ag nanoshell, with $\phi' = \pi/2$ being of special symmetry when using right- and left-circular-polarization vectors $(\hat{x} \mp i\hat{y})/\sqrt{2}$. Then the right and left αα components are exactly equal while the right and left α*G* are exactly opposite in sign, and similarly for α*A*. These results clearly do not hold at other geometries.

Nevertheless, we observe a key symmetry in the backscatter geometry for azimuthal angles ϕ' equal distances on either side of $\pi/2$. The right and left αα contributions switch values, while the others switch magnitudes and signs at the same time. Thus, further averaging the molecular position over ϕ' causes right

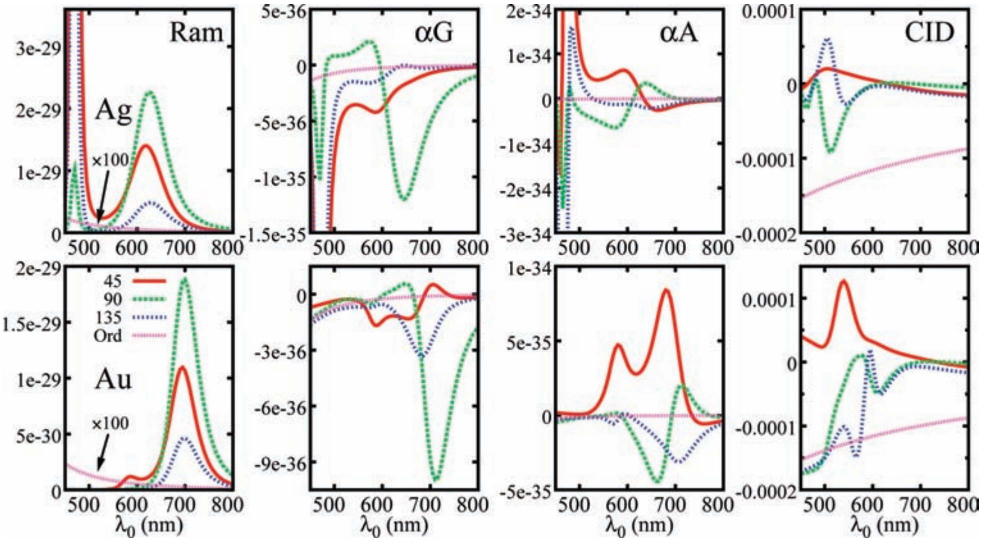

Figure 8. Signals calculated averaging both $|\mathbf{F}_R|^2$ and $|\mathbf{F}_L|^2$ over rotations and ϕ' for Ag (top row) and Au (bottom row) 40/50 nanoshells with molecules 1 nm outside. Column 1 corresponds to $|\mathbf{F}_R|^2 + |\mathbf{F}_L|^2$ (Raman). Columns 2 and 3 correspond to the α*G* and α*A* components of $|\mathbf{F}_R|^2 - |\mathbf{F}_L|^2$ (ROA). Column 4 corresponds to normalized CIDs (difference-over-sum). Variation with angle θ' at 45°, 90°, and 135° is illustrated in each case as well as ordinary (Ord) unenhanced analogs.

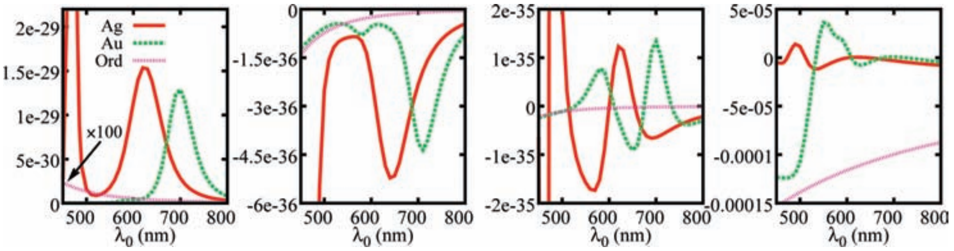

Figure 9. As in Figure 8 but with $|\mathbf{F}_R|^2$ and $|\mathbf{F}_L|^2$ also averaged over θ'.

TABLE 1: Decomposition of H_2S_2 Model Rotationally-Averaged Contributions to $|\mathbf{F}(\pi,0)|^2$ As Defined in eq 37 for SCP in Backscatter Geometry with a 40/50 nm Ag Nanoshell and with Incident Wavelength 700 nm[a]

ϕ'	$3\pi/8$	$\pi/2$	$5\pi/8$
αα	3.035233×10^{-30}	3.121081×10^{-30}	3.133382×10^{-30}
	3.133382×10^{-30}	3.121081×10^{-30}	3.035233×10^{-30}
α*G*	$-6.110034 \times 10^{-37}$	$-2.316612 \times 10^{-36}$	$-3.451463 \times 10^{-36}$
	3.451463×10^{-36}	2.316612×10^{-36}	6.110034×10^{-37}
α*A*	$-7.073764 \times 10^{-36}$	$-9.515487 \times 10^{-36}$	$-8.733283 \times 10^{-36}$
	8.733283×10^{-36}	9.515487×10^{-36}	7.073764×10^{-36}

[a] The molecular position around the nanoshell is at angle $\theta' = 5\pi/8$ and three different angles of ϕ'. The top number in each case is the contribution to $F_R(\pi,0)^2$ while the bottom number is the contribution to $|F_L(\pi,0)|^2$. Units are V^2.

and left differences to cancel for the αα case and to reinforce for the α*G* and α*A* cases. In other words, if there are uniform concentrations of the molecule around the nanoparticle, averaging over molecular angles ϕ' will be sufficient to guarantee that αα terms provide no contributions to the differential intensities.

This result holds for all orders of the Mie theory evaluations of the surface plasmon fields. There are further checks. For example, we find that removal of the nanoparticle brings right and left αα contributions into equality under rotational averaging alone, agreeing with ordinary ROA. For another, setting the dihedral angle χ to π, independently of averaging over ϕ', turns off the chirality and makes the rotationally averaged α*G* and α*A* terms vanish identically.

Figure 8 demonstrates the excitation wavelength dependence of the H_2S_2 ϕ'-averaged and rotationally averaged SCP-backscatter intensity contributions for both silver and gold 40/50 nanoshells at different values of the polar angle θ'. The bulk dielectric functions of both metals were taken from the data of Johnson and Christie.[51] As seen in the Raman intensities (column 1), there are nanoshell-dipole features to longer wavelengths and nanoshell-quadrupole features to shorter wavelengths. For the Johnson and Christie data, the nanoshell-quadrupole enhancements can peak higher for Ag, while the nanoshell-dipole enhancements usually dominate for Au.

The second column in Figure 8 contains the corresponding averaged α*G* contributions to the intensity differences, while the third column contains the corresponding α*A* contributions. It is seen that there are significant variations in the results for different θ' as well as for different wavelengths, and that the nanoshell-quadrupole mode can strongly affect the difference excitation profiles. This will be lessened in the event that the theoretical averaging is carried out over θ' and/or r'. As a general rule, it is borne out that α*A* contributions can exceed α*G* contributions, as discussed earlier, but this will depend on both geometry and wavelength. In the last column of Figure 8, normalized CIDs formed from averaged intensities are also calculated for different θ' and different excitation wavelengths λ_0 to assess their variability with different parameters. These are generally smooth in the nanoshell-dipole regions of the spectrum but considerably more variable in the nanoshell-quadrupole regions. Figure 9 shows the corresponding Ag and Au quantities with averages of $|\mathbf{F}_R|^2$ and $|\mathbf{F}_L|^2$ over θ' as well as ϕ' and rotations. While the nanoshell-dipole region of the α*G* excitation profile resembles the corresponding region of the Raman excitation profile (but reversed in sign), the corresponding α*A* profile turns out to be more complex for either metal. For both silver and gold, it appears that the nanoshell-dipole region of the CIDs is actually strongly reduced in magnitude, i.e., the averaged $I_R + I_L$ is enhanced more than the corresponding $I_R - I_L$. Averaging also over r' is not pursued here.

VI. Discussion

A formalism has been constructed for calculation of ROA enhancement in the case of (off-resonant) chiral molecules near plasmonic spherical nanoparticles. In these circumstances only electromagnetic enhancement (enhanced plasmonic density of states) needs to be considered. Mie theory and EM Green Tensor techniques have been extended to include molecular magnetic dipole and electric quadrupole fields, marrying the SERS scattering model of Kerker et al.,[22] with the ROA treatment by Barron and Buckingham.[7] The formalism was applied to a simple chiral-molecule model providing "derived" molecular response tensors including excitation wavelength dependence. It was then determined for backscatter configurations with isolated Ag and Au nanoshells that a combination of averaging over molecular rotations *and* molecular positions around the nanoshells ensures that $\alpha\alpha$ contributions to SEROA vanish. Furthermore, averaging over rotations alone ensures that αG and αA contributions vanish if the molecule is not chiral, i.e., a specific SEROA scenario has been theoretically confirmed to retain the chiral selectivity exhibited by normal ROA. Corresponding SEROA excitation profiles were calculated and analyzed, showing somewhat greater prominence of αA contributions than in ROA.

It is reasonable to expect that positional averaging will generally be necessary, though not sufficient, to obtain both enhancement and selectivity. Even for symmetric particles, there are immediately further questions. For which other detection geometries does the combination of rotational and positional averaging suffice to eliminate $\alpha\alpha$ differential scattering contributions? Regarding Figure 9, do other geometries have less disparity between the enhancements of $I_R + I_L$ and $I_R - I_L$? Is the situation described in this paper fundamentally altered for resonance ROA scattering? Deviating somewhat from spherical symmetry, can similar analyses be made for ellipsoidal particles? Such questions remain for future work.

Practical applications of SEROA will require consideration of fully adsorbed analytes. Many more potential complications then arise, e.g., incomplete analyte coating, inhibited rotations, surface heterogeneities, surface diffusion, directional substrates, temporal fluctuations and "chemical-effect" SERS influences. Proper characterization of adsorbed-molecule SEROA measurements is far beyond the scope of the present paper. Nevertheless, the results here are relevant to the extent that pure EM enhancement dominates chemical enhancement even in first-layer SERS. It now appears clear that, regardless of any other influences, the local field enhancements by themselves will contribute some $E1/E1$ components to differential scattering signals. That is, achiral molecules should generally be expected to contribute to CIDs in SEROA from adsorbates. However, there are currently no guidelines available for the relative magnitudes of achiral-versus-chiral contributions nor for their sensitivity to the extent of ensemble averaging.

Acknowledgment. This paper is dedicated to the extreme scientific enthusiasm of Robert W. Field that has enriched both the research community in general and work at MIT in particular. Conversations with B. E. Brinson, B. Janesko, S. Lal and P. Nordlander on SEROA are gratefully acknowledged. This material is based upon work supported by the U.S. DoD/ARO under the Multidisciplinary University Research Initiative (MURI) award W911NF-04-01-0203, by National Science Foundation Award No. CHE-0518476, and by the Robert A. Welch Foundation Award Nos. C-0016 and C-1685.

References and Notes

(1) Fleischmann, M.; Hendra, P.; McMillan, A. *Chem. Phys. Lett.* **1974**, *26*, 163.

(2) Jeanmarie, D. L.; Van Duyne, R. P. *J. Electroanal. Chem.* **1977**, *84*, 1.

(3) Moskovits, M. *Rev. Mod. Phys.* **1985**, *57*, 783.

(4) Otto, A.; Mrozek, I.; Grabhorn, H.; Akemann, W. *J. Phys. (Paris)* **1992**, *4*, 1143.

(5) Yonzon, C. R.; Stuart, D. A.; Zhang, X.; McFarland, A. D.; Haynes, C. L.; Van Duyne, R. P. *Talanta* **2005**, *67*, 438.

(6) Lal, S.; Link, S.; Halas, N. J. *Nat. Photonics* **2007**, *1*, 641.

(7) Barron, L. D.; Buckingham, A. D. *Mol. Phys.* **1971**, *20*, 1111.

(8) Barron, L. D.; Zhu, F.; Hecht, L.; Tranter, G. E.; Isaacs, N. W. *J. Mol. Struct.* **2007**, *834–6*, 7.

(9) Efrima, S. *Chem. Phys. Lett.* **1983**, *102*, 79.

(10) Efrima, S. *J. Chem. Phys.* **1985**, *83*, 1356.

(11) Hecht, L.; Barron, L. D. *Chem. Phys. Lett.* **1994**, *225*, 525.

(12) Hecht, L.; Barron, L. D. *J. Mol. Struct.* **1995**, *348*, 217.

(13) Kneipp, H.; Kneipp, J.; Kneipp, K. *Anal. Chem.* **2006**, *78*, 1363.

(14) Abdali, S. *J. Raman Spectrosc.* **2006**, *37*, 1341.

(15) Janesko, B. G.; Scuseria, G. E. *J. Chem. Phys.* **2006**, *125*, 124704.

(16) Etchegoin, P. G.; Galloway, C.; Le Ru, E. C. *Phys. Chem.: Chem. Phys.* **2006**, *8*, 2624.

(17) Abdali, S.; Johannessen, C.; Nygaard, J.; Nørbygaard, T. *J. Phys.: Condens. Matter* **2007**, *19*, 285205:1.

(18) Johannessen, C.; Abdali, S. *Spectroscopy* **2007**, *21*, 143.

(19) Bouř, P. *J. Chem. Phys.* **2007**, *126*, 136101.

(20) Abdali, S.; Blanch, E. W. *Chem. Soc. Rev.* **2008**, *37*, 980.

(21) Oldenburg, S. J.; Averitt, R. D.; Westcott, S. L.; Halas, N. J. *Chem. Phys. Lett.* **1998**, *288*, 247.

(22) Kerker, M.; Wang, D.-S.; Chew, H. *Appl. Opt.* **1980**, *19*, 4159.

(23) Trost, J.; Hornberger, K. *Chem. Phys.* **2007**, *355*, 115.

(24) Barron, L. D.; Hecht, L.; McColl, I. H.; Blanch, E. W. *Mol. Phys.* **2004**, *20*, 731.

(25) Brinson, B., Nonresonant Surface Enhanced Raman Optical Activity Ph. D. thesis, Rice University, 2009.

(26) Schatz, G. C.; Young, M. A.; Van Duyne, R. P. Electromagnetic Mechanism of SERS. In *Surface-Enhanced Raman Scattering: Physics and Applications*, Kneipp, K., Moskovits, M., Kneipp, H., Eds.;Springer: Berlin, 2006; Vol. 103, pp 19.

(27) Mie, G. *Ann. Phys.* **1908**, *25*, 377.

(28) Sarkar, D.; Halas, N. J. *Phys. Rev. E* **1997**, *56*, 1102.

(29) Ben-Menahem, A. *Proc. R. Soc. London A* **1989**, *426*, 79.

(30) Novotny, L.; Hecht, B. *Principles of Nano-Optics*; Cambridge University Press: New York, 2006.

(31) Aden, A. L.; Kerker, M. *J. Appl. Phys.* **1951**, *22*, 1242.

(32) Barron, L. D. *Molecular Light Scattering and Optical Activity*, 2nd ed.; Cambridge University Press: New York, 2004.

(33) Buckingham, A. D. *Adv. Chem. Phys.* **1967**, *12*, 107.

(34) Jackson, J. D. *Classical Electrodynamics*, 3rd ed.; John Wiley & Sons: New York, 1999.

(35) Luber, S.; Herrmann, C.; Reiher, M. *J. Phys. Chem. B* **2008**, *112*, 2218.

(36) Stratton, J. A. *Electromagnetic Theory*; John Wiley & Sons: New York, 2007.

(37) van de Hulst, H. C. *Light scattering by small particles*; Dover Publications: New York, 1957.

(38) Zurita-Sánchez, J. R.; Novotny, L. *J. Opt. Soc. Am. B* **2002**, *19*, 1355.

(39) Zurita-Sánchez, J. R.; Novotny, L. *J. Opt. Soc. Am. B* **2002**, *19*, 2722.

(40) Placzek, G. Rayleigh-Streuung und Raman-Effekt. In *Handbuch der Radiologie*; Marx, E, Ed.; Akademische Verlagsgesellschaft: Leipzig, 1934; Vol. 6, pp 205.

(41) Long, D. A. *Raman Spectroscopy*; McGraw-Hill: Maidenhead, G.B., 1977.

(42) Pecul, M.; Ruud, K. *Int. J. Quantum Chem.* **2005**, *104*, 816.

(43) Zuber, G.; Goldsmith, M.-R.; Beratan, D. N.; Wipf, P. *ChemPhysChem* **2005**, *6*, 595.

(44) Jensen, L.; Autschbach, J.; Krykunov, M.; Schatz, G. C. *J. Chem. Phys.* **2007**, *127*, 134101.

(45) Redington, R. L. *J. Mol. Spectrosc.* **1962**, *9*, 469.

(46) Marsden, C. J.; Smith, B. J. *J. Phys. Chem.* **1988**, *92*, 347.

(47) Nafie, L. A. *Annu. Rev. Phys. Chem.* **1997**, *48*, 357.

(48) Spencer, K. M.; Freedman, T. B.; Nafie, L. A. *Chem. Phys. Lett.* **1988**, *149*, 367.

(49) Hecht, L.; Che, D.; Nafie, L. A. *Appl. Spectrosc.* **1991**, *45*, 18.

(50) Hug, W. *Appl. Spectrosc.* **2003**, *57*, 1.

(51) Johnson, P. B.; Christy, R. W. *Phys. Rev. B* **1972**, *6*, 4370.

JP9037232